Cramér–Rao Bounds for 2-D Target Shape Estimation in Nonlinear Inverse Scattering Problems with Application to Passive Radar

Jong Chul Ye, *Member, IEEE*, Yoram Bresler, *Fellow, IEEE*, and Pierre Moulin, *Senior Member, IEEE*

***Abstract*—We present new methods for computing fundamental performance limits for two-dimensional (2-D) parametric shape estimation in nonlinear inverse scattering problems with an application to passive radar imaging. We evaluate Cramér–Rao lower bounds (CRB) on shape estimation accuracy using the domain derivative technique from nonlinear inverse scattering theory. The CRB provides an unbeatable performance limit for any unbiased estimator, and under fairly mild regularity conditions is asymptotically achieved by the maximum likelihood estimator (MLE). The resultant CRBs are used to define an asymptotic global confidence region, centered around the true boundary, in which the boundary estimate lies with a prescribed probability. These global confidence regions conveniently display the uncertainty in various geometric parameters such as shape, size, orientation, and position of the estimated target and facilitate geometric inferences. Numerical simulations are performed using the layer approach and the Nyström method for computation of domain derivatives and using Fourier descriptors for target shape parameterization. This analysis demonstrates the accuracy and generality of the proposed methods.**

***Index Terms*—Cramér–Rao bounds, Fourier descriptors, global confidence regions, nonlinear inverse scattering, passive radar imaging, shape estimation.**

I. Introduction

A VARIETY of engineering problems, including radar and sonar, involve estimation of the shape of an unknown object from scattering measurements collected at sensor elements. Imaging algorithms for such applications can broadly be divided into two classes: Fourier transform-based methods and nonlinear inverse scattering methods.

Fourier transform-based approaches are basically linearization techniques using the Born or physical-optics approximations [1]–[3]. Nonlinear inverse scattering methods make it possible to determine the nature of scatterers for frequencies in the *resonance regime*, where the wavelength is comparable to the size of the scatterers [2]. In this regime, conventional linear approximations such as Born and physical-optics do not hold, for these approximations require that the wavelength be much smaller than the size of the scatterers. Therefore, we must use the exact wave equation to obtain accurate solutions to nonlinear inverse scattering problems. This makes the problem of shape estimation in the resonance regime considerably more difficult than Fourier transform-based approaches.

Passive radar imaging, which is the main motivation for our study, is a nonlinear inverse scattering problem. Unlike traditional radar systems which transmit waveforms and deduce information about targets by measuring and analyzing the reflected signals, passive radar systems use "illuminators of opportunity" such as commercial television and AM/FM radio broadcasts to acquire target information [4], [5]. However, the waveforms used in commercial broadcasts have much lower frequencies compared to traditional active radar systems [5], [6]. For example, while active radar systems often operate in the centimeter wavelength range, the wavelength for lower VHF signals (55.25 – 79.25 MHz) is about 6 m. Such wavelengths are comparable to the size of common aircrafts and make the inverse problem severely nonlinear.

The major goals of this paper are to develop a parametric formulation of passive radar problems based on the nonlinear inverse scattering model and to establish fundamental performance limits of passive radar systems. The parametric formulation with a finite (usually small) number of parameters regularizes the solution to the ill-posed inverse problem, by imposing smoothness on the reconstructed boundary. It also provides the basis for an efficient maximum likelihood estimation algorithm. Once a suitable parametric model has been identified, fundamental bounds on the performance of shape estimation algorithms can in principle be derived, as was shown in the case of a linear inverse problem [7].

We conduct such an analysis for nonlinear inverse scattering problems using Cramér–Rao lower bounds (CRB). These bounds are widely used in problems where the exact minimum-mean-square error is difficult to evaluate. The CRB provides an unbeatable performance limit for any unbiased estimator and hence can be used to investigate the fundamental limits of parameter estimation problems or as a baseline for assessing the performance of a specific estimator. Furthermore, under fairly mild regularity conditions, the CRB is asymptotically achieved by the maximum likelihood estimator (MLE). Hence, the CRB can also serve as a predictor of the high signal-to-noise ratio (SNR) performance of the MLE and for bounding the accuracy of any other unbiased estimate.

Manuscript received October 12, 1999; revised November 9, 2000.

This work was supported by DARPA under Contract F49620-98-1-0498, administered by AFOSR, and by NSF under Contract CDA 96-24396.

J. C. Ye was with the Coordinated Science Laboratory, Department of Electrical and Computer Engineering, University of Illinois at Urbana-Champaign, Urbana, IL 61801 USA. He is now with Image Science Laboratory, Polaroid Corporation, Wayland, MA 02139 USA.

Y. Bresler and P. Moulin are with the Coordinated Science Laboratory, Department of Electrical and Computer Engineering, University of Illinois at Urbana-Champaign, Urbana, IL 61801 USA (e-mail: ybresler@uiuc.edu).

Publisher Item Identifier S 0018-926X(01)03646-8.

While CRBs are available for estimation of signal parameters such as target location [8]–[11], direction-of-arrival (DOA) [12]–[15], and size and orientation of a scatterer [16]–[18], only recently has this type of analysis been conducted for estimation of target shapes [7]. In [7], the boundary of a star-like target is parameterized using B-splines, and CRBs for the B-spline coefficients are computed for several shapes in a magnetic resonance imaging problem. However, the results in [7] are derived for a linear inverse problem; we are not aware of any similar result for nonlinear inverse scattering problems. Indeed, the problem is challenging, because in contrast with classical nonlinear signal processing problems where the map from parameters to measurements is explicit [19], the map here is given implicitly as the solution of a partial differential equation, which depends nonlinearly on the parameters.

This paper provides a new algorithm to compute CRBs for target shape estimation based on the domain derivative technique in nonlinear inverse scattering theory [2], [20]. Furthermore, we introduce a new approach to analyze and display the uncertainty in object recovery, in the form of asymptotic global confidence regions [21]. An asymptotic global confidence region has the form of a band (of varying width) created around the boundary and can be useful *a priori*, for purpose of design and analysis, as well as *a posteriori*, after measurements have been taken and the shape has been reconstructed, for assessing the reliability of the reconstruction. The availability of global confidence regions makes it possible to answer some basic questions about performance of passive radar systems, for example, which features of an object are difficult to estimate, or what is the effect of the transmitter and receiver locations.

To simplify the analysis in this paper, we assume throughout that the true shape is accurately described by the parametric model. In practice, a parametric inversion method will require estimation of the model order and will suffer from some mismatch between model and target. Consequently, our performance prediction may be optimistically biased.

For clarity, this paper focuses on estimation of a cylindrical symmetric target (whose profile is constant along the z-axis) with perfect electric conducting boundary, using transverse magnetic (TM) polarized incident plane waves [1], [22]. This setup gives rise to a relatively simple two-dimensional (2-D) imaging problem using the scalar Helmholtz equation. The extension to transverse electric (TE) polarized incident plane waves is in principle similar and is briefly addressed.

Section II sets up the parametric formulation of the nonlinear inverse scattering problem. Section III reviews the Cramér–Rao lower bound and introduces asymptotic global confidence regions as a new concept for the fundamental performance limits of target shape estimation. Section IV presents the domain derivative technique for the computation of CRB of shape parameters. The new algorithm requires the numerical solution of an exterior boundary value problem. We compute this solution with the Layer Approach and Nyström method, as reviewed in Section V. Section VI investigates passive radar applications and uses our algorithm to answer some relevant questions about the fundamental performance limits of passive radar systems. In particular, we provide numerical simulations using actual locations and carrier frequencies of commercial television stations in the Gaithersburg, MD area, where a prototype of Lockheed-Martin's Silent Sentry™ passive radar system is located. Section VII discusses an extension to TE polarized waves, and Section VIII concludes our discussion.

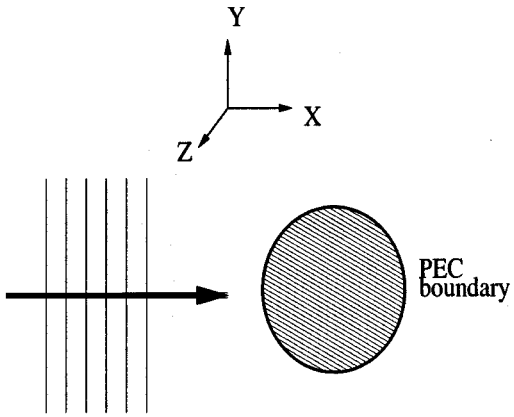

Fig. 1. An example of geometry of nonlinear inverse scattering problem using TM polarized plane incident wave.

II. Parametric Nonlinear Inverse Scattering Problem

A. Statistical Formulation

Nonlinear inverse scattering problems using the scalar Helmholtz equation have been well investigated in the literature (see [2] and the references therein). For example, such problems arise in electromagnetics, when a cylindrical symmetric perfect electric conducting object is illuminated with a transverse magnetic (TM) polarized plane wave [1]. For an object D with a bounded and connected boundary $\partial D = \mathbf{s}$ as shown in Fig. 1, the wave is completely characterized by the z-component of the electric field. Consider an incident electric field with z-component $u^i(\mathbf{x}) = \exp(jk\mathbf{x}\cdot\mathbf{d})$, where k is the wavenumber, the unit vector $\mathbf{d}$ is the direction of propagation, and $\mathbf{x} \in \mathbb{R}^2$ are 2-D coordinates. The total field can be represented by the sum of incident and scattered fields, $u = u^i + u^s$, and satisfies the 2-D scalar Helmholtz equation

$$\nabla^2 u + k^2 u = 0, \qquad \mathbf{x} \in \mathbb{R}^2 \setminus \overline{D} \tag{1}$$

with boundary condition

$$u = 0, \qquad \mathbf{x} \in \mathbf{s} \tag{2}$$

where $\overline{D}$ is the closure of domain D. In order for the solution to be unique and physically meaningful, the scattered wave u^s must satisfy the *Sommerfeld radiation condition* [23]

$$\lim_{|\mathbf{x}|\to\infty} \sqrt{|\mathbf{x}|}\left(\frac{\partial u^s}{\partial |\mathbf{x}|} - jku^s\right) = 0. \tag{3}$$

Throughout this paper, we express the scattered wave as a vector-valued function $\boldsymbol{\mathcal{F}}(\mathbf{s})$. Given N detectors located at $\mathbf{x}_i$, $i = 1, \ldots, N$, the function $\boldsymbol{\mathcal{F}}(\mathbf{s})$ is a N-dimensional column vector with complex elements $\mathcal{F}_i(\mathbf{s}) = u^s(\mathbf{x}_i)$:

$$\begin{aligned}\boldsymbol{\mathcal{F}}(\mathbf{s}) &= [\mathcal{F}_1(\mathbf{s}), \mathcal{F}_2(\mathbf{s}), \ldots, \mathcal{F}_N(\mathbf{s})]^T \\ &= [u^s(\mathbf{x}_1), u^s(\mathbf{x}_2), \ldots, u^s(\mathbf{x}_N)]^T.\end{aligned} \tag{4}$$

The elements of $\boldsymbol{\mathcal{F}}(\mathbf{s})$ then represent the "exact" values of the (z component of the) scattered waves for the assumed boundary $\mathbf{s}$. The measurements Y_i of the scattered wave $u^s(\mathbf{x}_i)$ for the ith detector are corrupted by additive noise

$$Y_i = \mathcal{F}_i(\mathbf{s}) + W_i, \qquad i = 1, \ldots, N \tag{5}$$

where W_i are independent zero mean complex Gaussian random variables with $N \times N$ covariance matrix

$$[\mathbf{C_W}]_{i,j} = \begin{cases} \sigma_i^2, & i = j \\ 0, & i \neq j \end{cases} \tag{6}$$

where σ_i^2 denotes the variance of real and imaginary components of the ith complex Gaussian random variable W_i. This noise model applies when the thermal noise of receivers dominates the measurement noise, or when the background noise is spatially homogeneous and Gaussian,[1] and the receivers are sufficiently separated to decorrelate the noise contributions. We organize the measurements as a single column vector of length N,

$$\mathbf{Y} = [Y_1, Y_2, \ldots, Y_N]^T. \tag{7}$$

The inverse scattering problem is then *to determine* $\mathbf{s}$ *from the measured value of* $\mathbf{Y}$.

B. Parametric Formulation of Shape Estimation Problems

We consider parametric shape representations of the form

$$\begin{aligned} \mathbf{s}(t) = \mathbf{s}(t; \boldsymbol{\phi}) &= [\, x(t) \quad y(t) \,]^T \\ &\triangleq \mathbf{B}(t)^T \boldsymbol{\phi} = \sum_{j=1}^{J} \mathbf{b}_j(t)\phi_j, \qquad t \in I \end{aligned} \tag{8}$$

where

t	index to points along the boundary taking values in a fixed interval $I = [0, T]$;
$\mathbf{b}_j(t) \in \mathbb{R}^2$	jth basis function indexed by t;
$\boldsymbol{\phi} = [\, \phi_1 \quad \cdots \quad \phi_J \,]^T \in \mathbb{R}^J$	J-dimensional parameter vector.

The functions $\mathbf{b}_j(t)$ are known, continuously twice-differentiable functions. Parameterizations such as Fourier descriptors (FD) [24], [25], B-splines [26], and wavelet descriptors [27], [28] are special cases of this model and have been widely used for shape representation. In our shape estimation problem, we assume that the true shape $\mathbf{s}(t)$ is accurately described by (8) with unknown $\boldsymbol{\phi}$. Furthermore, the model order J is assumed to be known *a priori*. Then, the original problem (5) is reduced to computing an estimate $\hat{\boldsymbol{\phi}}$ for $\boldsymbol{\phi}$, given the data (with a slight abuse of notation)

$$Y_i = \mathcal{F}_i(\boldsymbol{\phi}) + W_i, \qquad i = 1, \ldots, N. \tag{9}$$

[1]Even when the background noise is not inherently Gaussian, the Central Limit Theorem can be invoked to justify a Gaussian model for the measurement because it will usually be obtained by averaging sensor output over some observation time.

The boundary estimate is then

$$\hat{\mathbf{s}}(t) \triangleq \mathbf{s}(t; \hat{\boldsymbol{\phi}}). \tag{10}$$

In particular, we consider the maximum likelihood estimate of $\boldsymbol{\phi}$, which coincides, under the assumed Gaussian model, with the weighted least squares estimate

$$\hat{\boldsymbol{\phi}} = \arg\min_{\boldsymbol{\phi}} \|\mathbf{Y} - \boldsymbol{\mathcal{F}}(\boldsymbol{\phi})\|^2_{\mathbf{C}_{\boldsymbol{\phi}}^{-1}}. \tag{11}$$

In practice, the contour can only be approximated by a model of finite order J, and the optimum order must be estimated from the data along with the parameter themselves. This is analogous to the choice of a regularization parameter, and model order selection techniques [29]–[31] can be used to solve that problem. This issue, as well as the sensitivity of the estimates to model mismatch merit separate study and are left out of the analysis in this paper. In practice, our performance prediction may therefore be optimistically biased.

Parametric formulations (although more restricted than ours—see below) have been used before to compute a least square estimate $\mathbf{s}(t; \hat{\boldsymbol{\phi}})$ in nonlinear inverse scattering problems [2], [20].[2] Our goal here is to derive fundamental bounds on the performance of shape estimation in this context. This can be done via the Cramér–Rao lower bound (CRB) for estimates of $\boldsymbol{\phi}$, which is the subject of Section III.

C. Normalized Fourier Descriptors for Boundary Parameterization

This section introduces *Fourier Descriptors* (FD) [25], [32] as a specific example of the parameterization (8). One advantage of the FD parameterization is that smooth regular curves can usually be well represented by a relatively small number of coefficients, making the description more succinct. For this reason, FD's have been used extensively in pattern recognition and image processing [25], [32].

The FD parameterization has been used before in nonlinear inverse scattering problems to parameterize star-shaped objects centered at the origin of a coordinate system [2], [20]. The FD parameterization described in this section, however, is more general and can be used for arbitrarily located general-shape objects. More specifically, the boundary $\mathbf{s}(t) = [x(t), y(t)]^T$ is parameterized as

$$\begin{aligned} x(t) &= A_0 + \sum_{k=1}^{M} \{A_k \cos(kt) + A_{M+k} \sin(kt)\} \\ y(t) &= B_0 + \sum_{k=1}^{M} \{B_k \cos(kt) + B_{M+k} \sin(kt)\}, \\ & \qquad t \in I = [0, 2\pi] \end{aligned} \tag{12}$$

where $\{A_k, B_k\}$, $k = 0, \ldots, 2M$, are real FD parameters.

Unfortunately, the FD parameterization (12) is not unique. More specifically, for $t_0 \neq 0$, geometrically identical curves $\mathbf{s}(t)$ and $\mathbf{s}(t - t_0)$ have different FD parameters. Since the scattered wave is not affected by the starting point of the curve, the

[2]These formulations also assumed that the model order is given *a priori*.

nonuniqueness of the FD parameterization would lead to a degeneracy in the evaluation of the estimation performance.[3] This problem has been resolved by appropriate normalization with respect to the starting point of the curve in the case of complex FD's representation [33], [34]. This can be done by imposing the constraint $A_{M+1} = B_1 \geq 0$ in (12). Hence, the set of normalized FD coefficients has only $4M+1$ real-valued degrees of freedom (instead of $4M+2$ for the original FD coefficients) once the ambiguity due to the starting point has been removed. Therefore, the parameter vector $\boldsymbol{\phi}$ in (8) becomes $\boldsymbol{\phi} = \{A_0, \ldots, A_{2M}, B_0, B_2, \ldots, B_{2M}\} \in \mathbb{R}^{4M+1}$.

We conclude this section by noting that

$$\mathbf{s}_o = [A_0, B_0]^T \tag{13}$$

is the centroid of $\mathbf{s}$. Hence normalized FD's provide an efficient parameterization of the position and shape of a 2-D object, simultaneously.

III. Cramér–Rao Bounds and Global Confidence Regions

A. Cramér–Rao Bounds for Boundary Parameterization

According to the Cramér–Rao inequality, subject to some regularity conditions (which are satisfied in our estimation problem, as shown in Appendix B), the $J \times J$ covariance matrix of the estimation error $\hat{\boldsymbol{\phi}} - \boldsymbol{\phi}$ for the unknown parameter ϕ in the model (9) is bounded from below as [19]

$$\mathrm{Cov}(\hat{\boldsymbol{\phi}} - \boldsymbol{\phi}) \geq \mathbf{C}_{\boldsymbol{\phi}} \triangleq (\mathbb{I}_{\boldsymbol{\phi}})^{-1} \tag{14}$$

for *any unbiased* estimate $\hat{\boldsymbol{\phi}}$ of $\boldsymbol{\phi}$. Here, the matrix inequality notation $A \geq B$ indicates that $A - B$ is positive semidefinite, with A and B being Hermitian positive semidefinite matrices.

The matrix $\mathbb{I}_{\boldsymbol{\phi}}$ in (14) is the Fisher information matrix [6]

$$\mathbb{I}_{\boldsymbol{\phi}} = 2\mathrm{Re}\{\boldsymbol{\mathcal{F}}'(\boldsymbol{\phi})^H \mathbf{C}_{\mathbf{W}}^{-1} \boldsymbol{\mathcal{F}}'(\boldsymbol{\phi})\} \tag{15}$$

where $\mathbf{C}_{\mathbf{W}}$ denotes the covariance matrix given by (6). The Jacobian matrix $\boldsymbol{\mathcal{F}}'(\boldsymbol{\phi}) \in \mathbb{C}^{N \times J}$ is defined by

$$[\boldsymbol{\mathcal{F}}'(\boldsymbol{\phi})]_{i,j} = \frac{\partial \mathcal{F}_i(\boldsymbol{\phi})}{\partial \boldsymbol{\phi}_j} \tag{16}$$

and the superscript H denotes Hermitian transpose. Our first goal in this paper, is to develop a computationally efficient and numerically reliable way to compute (16) and hence the CRB for the boundary parameters. This is the subject of Sections IV and V.

B. Asymptotic Global Confidence Regions

In practice, because $\mathbf{s}(t)$ describes the geometry of an object, one is interested in assessing the quality of estimates of $\mathbf{s}(t; \boldsymbol{\phi})$ in easily interpreted geometric terms. Rather than the quality of estimates of $\boldsymbol{\phi}$ itself, what is needed is a global quality measure for the entire boundary $\{\mathbf{s}(t; \hat{\boldsymbol{\phi}}),\ \forall t \in I\}$. Such quantification of the uncertainty in shape estimation problems may answer many useful questions: what accuracy we can expect at any given point, which features of a shape are difficult to estimate, what is the effect of different parameterizations and data collecting geometries, etc.

Obtaining a geometrically meaningful global performance measure is, however, a challenging problem. While the estimate $\hat{\boldsymbol{\phi}}$ for unknown deterministic parameter $\boldsymbol{\phi}$ is a random vector, the estimate $\hat{\mathbf{s}}(t) = \mathbf{s}(t; \hat{\boldsymbol{\phi}})$ for unknown deterministic shape $\mathbf{s}(t; \boldsymbol{\phi})$ is a stochastic process continuously indexed by t. Following our recent work [21], we present a technique for constructing small-size global confidence regions in which the entire boundary estimate asymptotically lies with a given probability. These confidence regions can be conveniently visualized. They incorporate limits on the estimation performance for unknown geometric parameters such as shape, size, orientation, and the position of the object into an uncertainty band, which is created around the *true shape* $\mathbf{s}(t; \boldsymbol{\phi})$. Then, one can investigate the fundamental performance of shape estimation from the geometric properties of the confidence regions.

At this point, we make the following simplifying assumption. The dimension J of the unknown shape parameter $\boldsymbol{\phi}$ is small relative to the number of N of data available so that the asymptotic normality and efficiency properties of the maximum likelihood estimate (MLE) [19] approximately hold: the MLE $\hat{\boldsymbol{\phi}}$ is Gaussian-distributed with mean $\boldsymbol{\phi}$ and covariance $\mathbf{C}_{\boldsymbol{\phi}}$ given by (14). It then follows from the linear model (8) that the estimate $\hat{\mathbf{s}}(t)$ is a 2-D Gaussian stochastic process with mean $\mathbf{s}(t)$ and covariance matrix

$$\mathbf{C}_{\mathbf{s}}(t) \triangleq \mathrm{Cov}(\hat{\mathbf{s}}(t) - \mathbf{s}(t)) = \mathbf{B}^T(t) \mathbf{C}_{\boldsymbol{\phi}} \mathbf{B}(t). \tag{17}$$

Using (17), we define the CRB ellipse at location $\mathbf{s}(t)$

$$\mathcal{U}_\gamma(t) \triangleq \{\boldsymbol{\zeta} \in \mathbb{R}^2 \colon (\boldsymbol{\zeta} - \mathbf{s}(t))^T \mathbf{C}_{\mathbf{s}}(t)^{-1} (\boldsymbol{\zeta} - \mathbf{s}(t)) \leq \gamma^2\}, \tag{18}$$

where γ is a parameter that quantifies the size of the CRB ellipse. Hence, $\mathcal{U}_\gamma(t)$ corresponds to uncertainty about the estimate of $\mathbf{s}(t)$ at t. We generate a global confidence region by moving the CRB ellipse along the boundary (Fig. 2):

$$\mathcal{U}_\gamma \triangleq \bigcup_{t \in I} \mathcal{U}_\gamma(t). \tag{19}$$

The region $\mathcal{U}_\gamma$ forms a "tube" around the true boundary $\mathbf{s}(t)$. We would like to relate the size parameter γ in (18) to the probability (confidence level) that the whole boundary estimate $\{\hat{\mathbf{s}}(t), \forall t \in I\}$ lies in the global confidence region

$$P_{\mathcal{U}} \triangleq \Pr\{\hat{\mathbf{s}}(t) \in \mathcal{U}_\gamma,\ \forall t \in I\}. \tag{20}$$

This probability turns out to be difficult to evaluate, as it requires the level crossing statistics of a 2-D nonstationary stochastic

[3] The Fourier descriptors for *star-shaped objects* in [2] and [20] are, however, invariant to the starting point of the curve since the FD's only parameterize the radial direction of the curve.

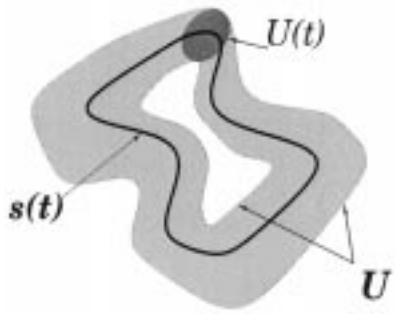

Fig. 2. Equal-probability contour (CRB ellipse) and confidence regions for target boundary.

process $\hat{\mathbf{s}}(t)$ [21]. Instead, we use the following lower bound[4] on $P_{\mathcal{U}}$ [21]:

$$\Pr\{\hat{\mathbf{s}}(t) \in \mathcal{U}_\gamma,\, \forall\, t \in I\} \geq 1 - (1+\kappa\gamma)\exp\left(-\frac{\gamma^2}{2}\right) \quad (21)$$

where the problem-dependent constant κ is given by

$$\kappa \triangleq \int_0^T \left(\frac{\zeta(t)}{2\pi}\right)^{1/2} dt \quad (22)$$

$$\zeta(t) = \text{trace}\{\mathbf{P}^{\perp}\dot{\mathbf{A}}\mathbf{A}^{\dagger}\mathbf{A}^{\dagger}\dot{\mathbf{A}}\mathbf{P}^{\perp}\} \quad (23)$$

$$\mathbf{A} = \mathbf{C}_{\boldsymbol{\phi}}^{1/2}\mathbf{B}(t) \quad (24)$$

$\mathbf{P}^{\perp}$ denotes the projection unto the null space of $\mathbf{A}^T$, $\dot{\mathbf{A}}$ denotes the derivative of $\mathbf{A}$ with respect to t, and $\mathbf{A}^{\dagger}$ denotes the pseudo-inverse of $\mathbf{A}$. Therefore, for a given global confidence level $P_{\mathcal{U}}$, the corresponding value of γ can be computed by solving a nonlinear equation for γ

$$(1+\kappa\gamma)\exp\left(-\frac{\gamma^2}{2}\right) = 1 - P_{\mathcal{U}}. \quad (25)$$

IV. The Domain Derivative Approach for Computing the CRB

A. The Domain Derivative

One concept that we use extensively, is the *domain derivative* of the mapping $\boldsymbol{\mathcal{F}}$ [20]. This refers to the infinitesimal variation of the mapping $\boldsymbol{\mathcal{F}}(\mathbf{s})$ with respect to an infinitesimal change of boundary $\mathbf{s}$. The domain derivative is an essential component for computing the gradient of a mapping $\boldsymbol{\mathcal{F}}$ with respect to boundary changes and has been successfully employed in Newton-type inversion algorithms for nonlinear inverse scattering problems [20].

To exploit established results for the domain derivative, we confine our attention to boundaries of class C^2 [35]. The boundary $\mathbf{s}$ of a bounded domain D is of class C^2 if the boundary admits a representation in terms of twice differentiable coordinate functions $x(t)$ and $y(t)$ for $t \in I$

$$\mathbf{s}(t) = [x(t),\, y(t)]^T \quad (26)$$

[4]A similar lower bound holds for the probability that the true shape lies in an *a posteriori* confidence region $\hat{\mathcal{U}}_\gamma$ defined around the maximum likelihood estimate $\hat{\mathbf{s}}(t)$ [21].

and $[x'(t)]^2 + [y'(t)]^2 > 0$ where the "prime" denotes the derivative with respect to t. We call such a curve a *regular curve* since it does not have corners or cusps [35], [36].

Now consider a shape $\mathbf{s}$, a vector field $\mathbf{q}(\mathbf{x})$, $\mathbf{x} \in \mathbf{s}$, and define the deformation

$$\mathbf{s}_{\epsilon\mathbf{q}} = \{\mathbf{x} + \epsilon\mathbf{q}(\mathbf{x}) \colon \mathbf{x} \in \mathbf{s}\}. \quad (27)$$

It is assumed that the vector field $\mathbf{q}(\mathbf{x})$ is continuously twice-differentiable so that $\mathbf{s}_{\epsilon\mathbf{q}}$ is still of class C^2 [20]. Next define the domain derivative of $\boldsymbol{\mathcal{F}}$ at $\mathbf{s}$ during the deformation by

$$\boldsymbol{\mathcal{F}}'(\mathbf{s};\, \mathbf{q}) = \lim_{\epsilon \to 0} \frac{1}{\epsilon}[\boldsymbol{\mathcal{F}}(\mathbf{s}_{\epsilon\mathbf{q}}) - \boldsymbol{\mathcal{F}}(\mathbf{s})]. \quad (28)$$

If the limit exists, $\boldsymbol{\mathcal{F}}'(\mathbf{s};\, \mathbf{q})$ corresponds to the rate of change in the scattered wave due to the deformation. The following theorem establishes the existence of the limit.

Theorem 1 [20]: Let $\mathbf{s}$ be of class C^2, its deformation $\mathbf{s}_{\epsilon\mathbf{q}}$ be given by (27) and be also of class C^2, and u^0 be the solution of the scattering problem (1). Then, the domain derivative $\boldsymbol{\mathcal{F}}'(\mathbf{s};\, \mathbf{q})$ exists and is given by the solution u to the Helmholtz equation in $\mathbb{R}^2 \setminus \overline{D}$ satisfying the Sommerfeld radiation condition (3) and the boundary condition

$$u = -\boldsymbol{\nu} \cdot \mathbf{q}\frac{\partial u^0}{\partial \boldsymbol{\nu}} \text{ on } \mathbf{s} \quad (29)$$

where $\boldsymbol{\nu}$ denotes the outer unit normal vector on $\mathbf{s}$.

B. Application of the Domain Derivative for CRB Computation

The Fisher information matrix in (15) (and the CRBs) can be successfully computed using the domain derivative technique. Without the domain derivative technique, extensive inversion simulations would be required to compute empirical shape estimation error bounds. A simple application of Kirsch's Theorem 1 provides, as proved in Appendix A, an explicit way to compute (16).

Corollary 1: For the general linear parametric boundary model $\mathbf{s}(t;\boldsymbol{\phi})$ in (8) where $\mathbf{b}_j(t)$, $j = 1, \ldots, J$ are continuously twice-differentiable, the mapping $\boldsymbol{\mathcal{F}}$ is differentiable with $\partial\mathcal{F}_i(\boldsymbol{\phi})/\partial\phi_j = u_j'(\mathbf{x}_i)$ for $i = 1, \ldots, N$ and $j = 1, \ldots, J$. Here, u_j' is given by the solution of the Helmholtz equation in $\mathbb{R}^2 \setminus \overline{D}$ satisfying the Sommerfeld radiation condition and the boundary condition

$$u_j'(\mathbf{s}(t)) = -\boldsymbol{\nu}(t) \cdot \mathbf{b}_j(t)\frac{\partial u^0}{\partial \boldsymbol{\nu}(t)}, \qquad t \in I \quad (30)$$

where $\boldsymbol{\nu}(t)$ and $\mathbf{b}_j(t)$ denote the outer unit normal vector on $\mathbf{s}(t)$, and the jth basis function in the parameterization (8), respectively, and u^0 is the solution of the scattering problem (1).

For the FD parameterization of Section II-C, we have $\boldsymbol{\phi} = \{A_0, \ldots, A_2, B_0, B_2, \ldots, B_{2M}\} \in \mathbb{R}^{4M+1}$. According to Corollary 1, the domain derivatives can then be computed by solving the Helmholtz equation in $\mathbb{R}^2 \setminus \overline{D}$ satisfying the Sommerfeld radiation condition and the boundary condition

$$u_j'(\mathbf{s}(t)) = \frac{\Lambda(t,\, \phi_j)}{\sqrt{(x'(t))^2 + (y'(t))^2}}\,\frac{\partial u^0}{\partial \boldsymbol{\nu}(t)}, \qquad t \in [0,\, 2\pi] \quad (31)$$

where

$$\Lambda(t, \phi_j) = \begin{cases} -y'(t)\cos(kt), & \text{for } \boldsymbol{\phi}_j = A_k \\ & (k = 0, \ldots, M) \\ -y'(t)\sin(t) + x'(t)\cos(t), & \text{for } \boldsymbol{\phi}_j = A_{M+1} \\ -y'(t)\sin(kt), & \text{for } \boldsymbol{\phi}_j = A_k \\ & (k = M+2, \ldots, 2M) \\ x'(t), & \text{for } \boldsymbol{\phi}_j = B_o \\ x'(t)\cos(kt), & \text{for } \boldsymbol{\phi}_j = B_k \\ & (k = 2, \ldots, M) \\ x'(t)\sin(kt), & \text{for } \boldsymbol{\phi}_j = B_k \\ & (k = M+1, \ldots, 2M). \end{cases} \tag{32}$$

C. Multispectral Sensors

The domain derivative technique can be extended to the case when the incident fields have multiple frequencies. Section VI shows one such application of this model, in passive radar imaging. The extension of model (9) to multiple-frequency illuminators is given by

$$Y_{i,l} = \mathcal{F}_{i,l}(\boldsymbol{\phi}) + W_{i,l} \tag{33}$$

for $i = 1, \ldots, N_l$, $l = 1, \ldots, L$ and $N = \sum_{l=1}^{L} N_l$, where L denotes the number of distinct frequency bands and N_l is the number of sensor measurements from the lth frequency illuminator. Assuming that the random variables $W_{i,l}$ are independent, the Fisher information matrix takes the form

$$\mathbb{I}_{\boldsymbol{\phi}} = \sum_{l=1}^{L} \mathbb{I}_{l,\boldsymbol{\phi}} \tag{34}$$

where $\mathbb{I}_{l,\boldsymbol{\phi}}$ denotes the Fisher information matrix for the lth frequency band measurements. Now the Fisher information matrix $\mathbb{I}_{l,\boldsymbol{\phi}}$ can be computed using Corollary 1 by substituting the wavenumber k of the wave equation (1) by the lth wavenumber k_l.

V. Computation of Domain Derivatives

In the preceding sections, we used the domain derivative to derive an expression for the CRB on boundary parameters and obtain global confidence regions. We also showed that this domain derivative can be computed by solving the Helmholtz equation with an appropriate boundary condition (30). The numerical solution of this equation, however, presents two difficulties, which must be carefully addressed.

Usually, the method of integral equations is preferred for solving boundary value problems. Indeed, this method automatically satisfies the specified boundary conditions as well as the Sommerfeld radiation condition (3) once an appropriate Green's function has been selected [1], [2], [35]. The resulting integral equations are usually of the second kind. However, the solution to such integral equations is nonunique if there exists a nontrivial solution u to the Helmholtz equation in the interior domain D, where u satisfies homogeneous Neumann boundary conditions $\partial u/\partial \boldsymbol{\nu} = 0$ on $\mathbf{s}$ [2]. A variety of devices have been designed in the literature for overcoming the nonuniqueness difficulties of the integral equation approach. The most attractive method in this respect is the *layer approach* [2], which combines two integral equations and is the one we use.

Another difficulty in implementing the domain derivative is the discretization issue. Integral equations have singularities due to the Green's function. These singularities introduce numerical difficulties when the integral equations are discretized. To overcome the difficulties, a variety of techniques have been used in the literature, depending on the method used for approximating the singularities. This paper employs the *Nyström method*. This method separates singularities from analytic parts and then approximates the integral equation using a quadrature rule and a trapezoidal rule. Here, the discretization is done along the one-dimensional (1-D) quadrature points. The main advantage of the Nyström method is that it is generally accurate, stable, and preserves the condition number of the integral operator, whereas in other methods the condition number can be disturbed by a poor choice of basis [37].

We have employed the layer approach and the Nyström method to compute the domain derivative. We note, in passing, that several additional complications arise when attempting to extend the work of this paper to three-dimensional (3-D) problems. Among them is that the layer approach and Nyström method may not be effective. For example, there is no straightforward quadrature rule available dealing appropriately with the singularity of the 3-D Green's function. Hence, here the Nyström method loses some of its attractiveness. This topic is beyond the scope of this paper, however, and interested readers are referred to classical references, such as [38].

VI. Numerical Results

In this section, we consider the FD parameterization of Section II-C, and compute CRBs under two different scenarios. The first numerical study compares an analytical expression for the CRB on the estimation of the radius of a cylinder with the numerical CRB computed by our new algorithm. The results illustrate the numerical accuracy of our method. The second study computes CRBs for the FD coefficients and demonstrates confidence regions for a 2-D, aircraft-like target.

A. Experiment 1: Cylinder Radius Estimation

Referring to Fig. 3, consider a TM polarized plane wave whose electric field has z-component $u^i(\mathbf{x}) = \exp(jk\mathbf{x} \cdot \mathbf{d})$ with $\mathbf{d} = (\cos\theta_0, \sin\theta_0)$ and is incident on a cylinder with radius ρ centered at the origin. We think of ρ as a scalar parameter that parameterizes the shape of the object. We observe a noisy version of the scattered wave $u^s(\mathbf{x})$ using a single sensor at the location

$$\mathbf{x} = (R\cos\theta, R\sin\theta). \tag{35}$$

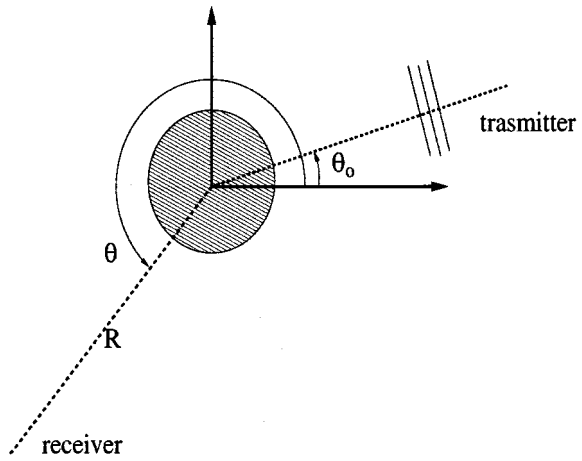

Fig. 3. Geometry of the first example. A cylinder of radius ρ is illuminated from direction $\mathbf{d} = (\cos\theta_0, \sin\theta_0)$ using a TM polarized plane wave. The CRB for the radius is computed by rotating a receiver located in $\mathbf{x} = (R\cos\theta, R\sin\theta)$.

The scattered wave is given by [22], [39]

$$u^s(\mathbf{x}) = -\sum_{n=-\infty}^{\infty} j^n \frac{J_n(k\rho)}{H_n^{(1)}(k\rho)} H_n^{(1)}(kR) e^{jn(\theta-\theta_o)} \quad (36)$$

where $J_n(\cdot)$ denotes the Bessel function of order n. The gradient of $u^s(\mathbf{x})$ with respect to ρ can be computed by

$$\frac{\partial u^s(\mathbf{x})}{\partial \rho} = \frac{2j}{\pi\rho} \sum_{n=-\infty}^{\infty} \frac{j^n}{(H_n^{(1)}(k\rho))^2} H_n^{(1)}(kR) e^{jn(\theta-\theta_o)} \quad (37)$$

using the properties of Bessel functions. Hence, for a sensor at location $\mathbf{x}$ in (35) with noise variance $\mathbf{C_W} = \sigma^2$, the CRB (14) on radius estimation is given by

$$\mathbf{C}_\rho = \frac{\sigma^2}{2}\left[\left(\frac{\partial u^s(\mathbf{x})}{\partial \rho}\right)^* \frac{\partial u^s(\mathbf{x})}{\partial \rho}\right]^{-1} \quad (38)$$

where the superscript $*$ denotes the complex conjugate.

In our numerical study, the receiver is located at a distance $R = 1000$ m from the target, the frequency of the plane wave is 50 MHz, and the direction of illumination is $\theta_0 = 180°$. In Fig. 4(a) and (b), we plot $\mathbf{C}_\rho$ of (38) as a function of receiver angle θ for a perfect electric conducting cylinder of radius $\rho =$ 1 m and $\rho = 10$ m, respectively, assuming that the measured signal at each θ is normalized to 20 dB signal to noise ratio (SNR). The SNR is defined by

$$\text{SNR (dB)} = 20\log\left(\frac{|u^s(\mathbf{x})|^2}{\sigma^2}\right). \quad (39)$$

Here, σ^2 is adjusted for each θ to obtain a fixed SNR $= 20$ dB. This is achieved by computing the scattered field $u^s(\mathbf{x})$ for each θ. Fig. 4(a) and (b) also shows the $\mathbf{C}_\rho$ computed by the new algorithm based on the domain derivative. Since the shape $\mathbf{s}$ is a circle, the FD coefficients in (12) are

$$A_1 = B_{M+1} = \rho, \qquad A_k = B_k = 0 \text{ (otherwise)} \quad (40)$$

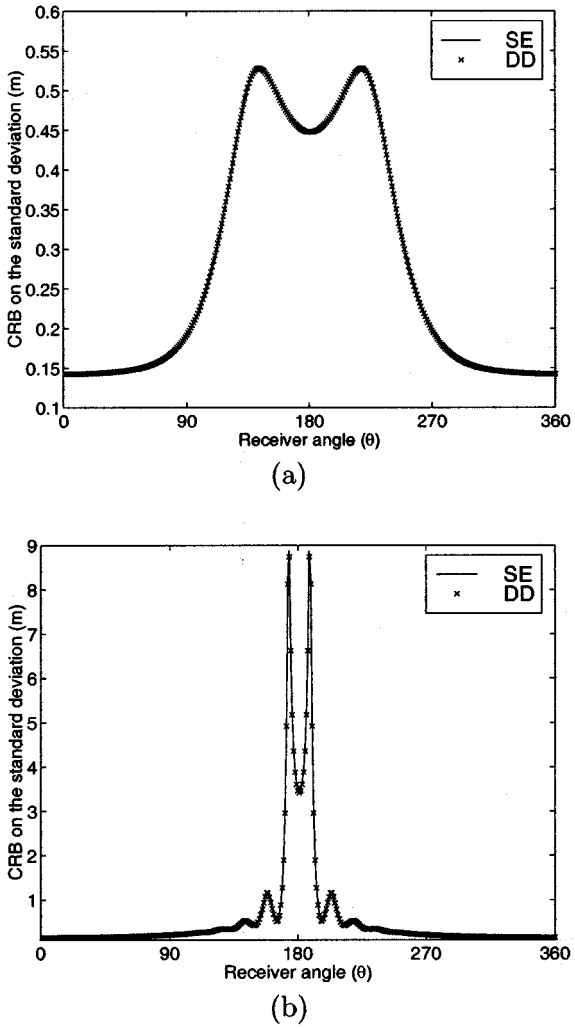

Fig. 4. CRB for estimation of cylinder radius ρ. Comparison of the explicit form CRB using Bessel function series expansion (SE) (37) with the numerical CRB obtained using the domain derivative (DD). (a) $\rho = 1$ m, and (b) $\rho =$ 10 m. The measurement SNR at the sensor is equally set to 20 dB for all θ and the frequency of the illumination is 50 MHz.

allowing only one degree of freedom. A total of 720 quadrature points are used for the discretization of the integral equation by the Nyström method.[5] The value of $\mathbf{C}_\rho$ is computed at every 1° angle. The total computation time for 360 values of the $\mathbf{C}_\rho$ was about 5 min. on a Sun Sparc Ultra 5 station. We observe that our numerical algorithm accurately matches the explicit formulas (37) and (38).

B. Experiment 2: Estimation of Aircraft Shape and Location

We now compute CRBs for shape and location estimation of aircraft-like 2-D objects using the actual locations and carrier frequencies of 20 commercial television stations near Gaithersburg, MD. Fig. 5 depicts a 2-D aircraft-like target whose con-

[5]Since the radii of cylinders are $\rho = 1$ m and $\rho = 10$ m at 50 MHz operating frequency, 720 quadrature points corresponds to the sampling steps about 1/700 or 1/70 of the wavelength, respectively. Considering that 10 to 20 samples per wavelength are usually used, the sampling densities in this paper are quite high. We have chosen these high sampling densities in order to prevent any discretization error from interfering with our analysis since we are studying with fundamental performance limit of inverse problems rather than forward problems.

TABLE I
FOURIER-DESCRIPTER COEFFICIENTS FOR THE AIRCRAFT-LIKE 2D TARGET IN FIG. 5 ($A_0 = B_0 = 0$)

Index (k)	1	2	3	4	5	6	7
A_k	2.059e+3	-5.234e+1	3.034e+2	1.914e+2	3.422e+1	1.752e+2	1.482e+2
A_{M+k}	5.178e-0	1.638e+1	-1.144e-1	-2.629e-0	-2.069e-0	-6.305e-1	1.224e-1
B_k	5.178e-0	-1.935e+1	1.839e+1	-2.518e+1	6.657e-0	-8.305e-0	6.141e-1
B_{M+k}	1.531e+3	4.236e+2	9.141e+1	-7.035e+2	2.098e+2	7.042e+1	1.085e+2

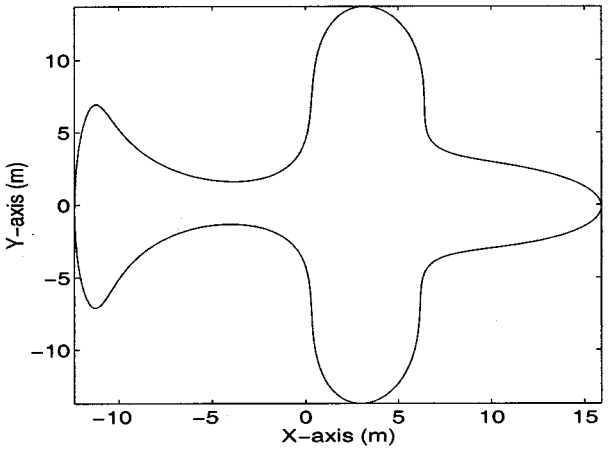

Fig. 5. Aircraft-like 2-D target generated by Fourier-Descriptor coefficients from Table I ($M = 7$).

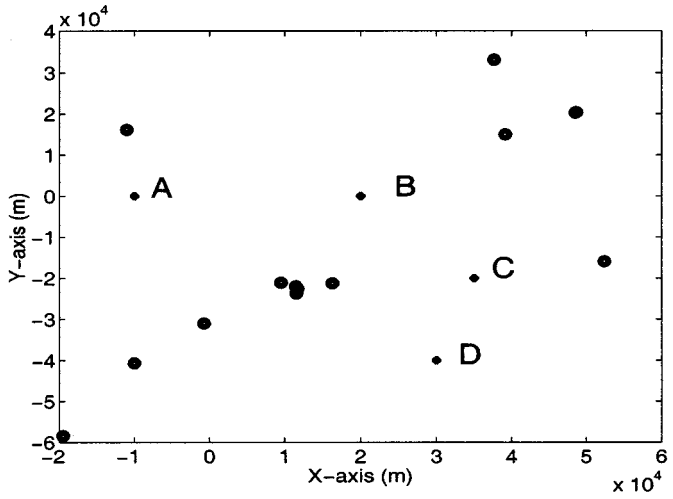

Fig. 6. Two-dimensional locations of commercial television stations in Gaithersburg. The origin of the coordinates corresponds to the location of Lockheed-Martin's Silent Sentry™ prototype, and the points A–D denote target locations.

tour is generated using the Fourier descriptor representation (12) with $M = 7$. The 29 FD coefficients are given in Table I. Again, we have used the constraint $A_{M+1} = B_1$ to avoid the ambiguity due to the starting point. Fig. 6 shows the actual locations of the television stations. The origin of the coordinate system is the location of Lockheed-Martin's Silent Sentry™ prototype, which corresponds to the receiver. Table II shows the X–Y position and the carrier center frequency of each station. We assume that the transmitted signal is a TM polarized plane wave. The SNR for each received signal is set equal to 10 dB by adjusting the

TABLE II
POSITIONS AND CENTER FREQUENCIES OF COMMERCIAL TELEVISION AND RADIO STATIONS NEAR GAITHERSBURG, MD. THE ORIGIN OF THE COORDINATE SYSTEM CORRESPONDS TO THE LOCATION OF A PROTOTYPE OF LOCKHEED-MARTIN'S SILENT SENTRY™

Station	X-coordinate (km)	Y-coordinate (km)	Frequency (MHz)
WBDC	16.298	-21.239	687
WRC	11.542	-23.711	67
WTTG	11.470	-21.952	77
WJLA	11.713	-22.564	175
WUSA	11.713	-22.564	187
WDCA	9.521	-21.083	507
WETA	9.521	-21.083	543
WHMM	9.521	-21.083	579
WMPT	52.400	-15.918	519
WBFF	48.671	20.382	657
WNUV	39.150	14.972	711
WHSW	39.150	14.972	531
WMAR	48.577	20.226	55
WBAL	48.577	20.226	199
WJZ	48.577	20.226	211
WMPB	37.657	33.095	789
WFPT	-11.035	16.152	759
WNVC	-0.719	-31.013	723
WNVT	-19.471	-58.408	705
WNVI	-10.004	-40.653	783

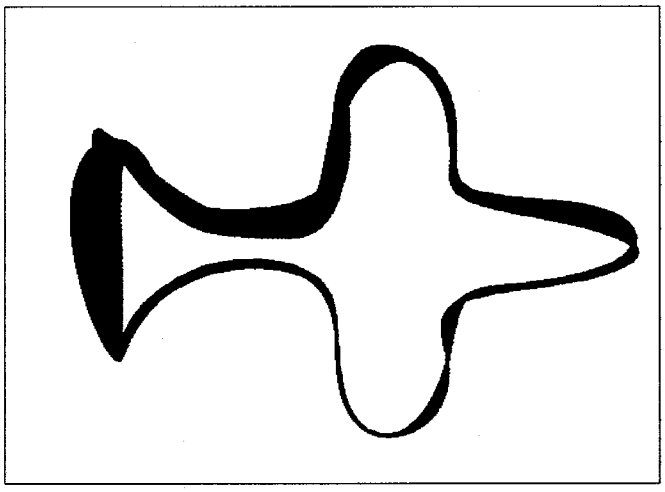

Fig. 7. Illustration of the $P_{\mathcal{U}} \geq 97\%$ confidence region for shape estimation of the aircraft-like target, located at the A-mark in Fig. 6.

value of σ_i^2 of the noise covariance matrix $\mathbf{C_W}$ in (6), as explained in Section VI-A. The data in this case contain multi-frequency information, and the expression (34) for multi-spectral sensors is used to account for this. Even though there are 20 transmitters, there are only 14 distinct transmitter locations: for

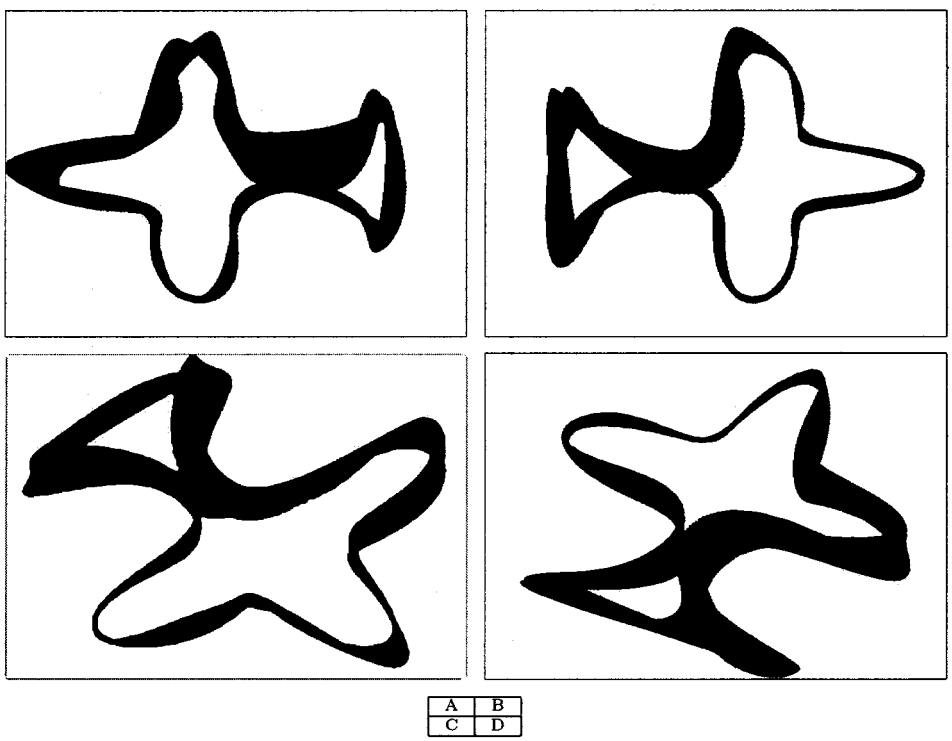

Fig. 8. Illustration of $P_{\mathcal{U}} \geq 97\%$ confidence regions when the target is located at the A–D marks in Fig. 6, respectively.

TABLE III
CRB ON THE STANDARD DEVIATIONS FOR FD COEFFICIENTS WHEN TARGET IS LOCATED AT THE A-MARK IN FIG. 6 WITH ORIENTATION SHOWN IN FIG. 7

Index (k)	0	1	2	3	4	5	6	7
A_k	0.130	0.103	0.062	0.115	0.086	0.058	0.075	0.126
A_{M+k}	N/A	0.093	0.159	0.077	0.084	0.048	0.086	0.107
B_k	0.067	N/A	0.228	0.211	0.117	0.212	0.259	0.050
B_{M+k}	N/A	0.124	0.067	0.130	0.039	0.144	0.095	0.122

example, the stations WDCA, WETA, WHMM are located at the same coordinate. This is because some commercial stations transmit on multiple channels. However, for the multispectral CRB computation, each channel with different carrier frequency corresponds to distinct data, so we have 20 distinct broadcast signals.

Table III gives the CRB on the error standard deviations for the 29 FD coefficients when the aircraft is located at the A-mark in Fig. 6. In Fig. 7, the global confidence region with probability $P_{\mathcal{U}} \geq 97\%$ for the aircraft boundary is illustrated. The corresponding size parameter γ in (18) is determined by solving (25). Observe that the estimation of the upper-left boundary is less accurate than the lower-right boundary. This phenomenon can be understood by considering the location of the transmitters and the receiver: only one commercial station (WFPT) is located northeast of the aircraft. This can be observed again in Fig. 8(a)–(d), which gives the global confidence regions for an aircraft located at the A–D marks in Fig. 6 with different orientations.

To investigate the effect of the wavelength of the transmitted signals as well as bandwidth, we momentarily consider an hypothetical scenario where all twenty stations transmit signals at the same frequency. As observed in Table II, there are only 14 distinct locations of commercial stations in Gaithersburg, so only 28 different real measurements (or 14 complex measurements) are available for the single-frequency scenario. It becomes impossible to reliably estimate the 29 unknown parameters in the normalized FD representation. Therefore, in this case, we assume that the position of the aircraft, $\mathbf{s}_o = [A_o, B_o]^T$, is known, reducing the number of unknown parameters to 27. Fig. 9(b)–(d) present $P_{\mathcal{U}} \geq 97\%$ global confidence regions for the single-frequency stations with 199 MHz, 519 MHz, and 789 MHz, respectively, when the aircraft is located at the A-mark in Fig. 6. In this case, higher frequency signals provide improved estimation performance, while with low-frequency signals such as 199 MHz, shape estimation is completely unreliable. Estimation performance is worst in the upper-left part of the boundary, which is directly illuminated by only one station (WFPT). The wavelength of the 199 MHz signal is about 1.5 m, which is comparable to the width of the narrowest part of the aircraft boundary. Apparently, the measurement due to the isolated station in the northwest (WFPT) does not convey enough information about that part of the boundary. This results in a nearly singular Fisher information matrix and in a very large global confidence region, as shown in Fig. 9(b). The influence of signal bandwidth is demonstrated in Fig. 9(a), where we provide $P_{\mathcal{U}} \geq 97\%$ global confidence regions using the actual frequencies of the transmitters listed in Table II. Here again the position of the target is assumed known, to facilitate comparison with Fig. 9(b)–(d). We observe that the use of multiple-frequency illuminators provides significantly improved estimation performance. Comparing with Fig. 7, we also note that, as might have been expected, fixing the position reduces error bounds.

In the simulations, a total of 720 quadrature points were again used for the discretization of the integral equation by the Nys-

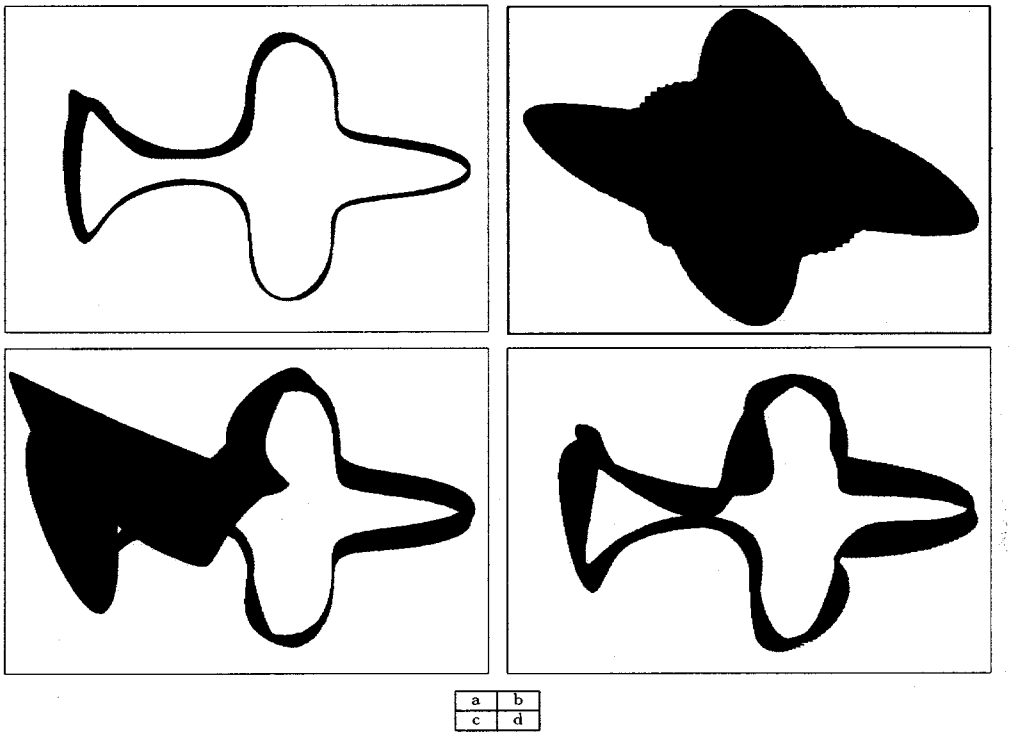

Fig. 9. Illustration of $P_{\mathcal{U}} \geq 97\%$ confidence regions due to (a) multi-frequency stations given in Table II, and single-frequency stations with frequencies of (b) 199 MHz, (c) 519 MHz, and (d) 789 MHz, respectively. In this simulation, the target is located at the A-mark in Fig. 6, and its location is considered known.

tröm method. The total computation times for the CRBs were about 40 min for a multispectral simulation and 5 min for a single frequency simulation on a Sun Ultra Sparc 5 station.

VII. Extension to TE Polarization

Another useful extension of the global confidence region analysis is the estimation of a cylindrical symmetric target (whose profile is constant along the z-axis) with perfect electric conducting boundary, using transverse electric (TE) polarized incident plane waves [1], [22]. This setup again gives rise to a relatively simple 2-D imaging problem using the scalar Helmholtz equation (1) with a Neumann boundary condition

$$\frac{\partial u}{\partial \boldsymbol{\nu}} = 0, \qquad \text{on } \mathbf{s}. \tag{41}$$

For the TE case, we can again compute the domain derivative as a solution to a wave equation, as stated in Proposition 1. The proof may be found in Appendix C.

Proposition 1: Let $\mathbf{s}$ be of class C^2, its deformation $\mathbf{s}_{\epsilon\mathbf{q}}$ be given by (27) and be also of class C^2, and u^0 be the solution of the scattering problem (1). Then, the domain derivative of u^0 exists and is given by the solution u to the Helmholtz equation in $\mathbb{R}^2 \setminus \overline{D}$ satisfying the Sommerfeld radiation condition (3) and the boundary condition

$$\frac{\partial u}{\partial \boldsymbol{\nu}} = \nabla \cdot ((\boldsymbol{\nu} \cdot \mathbf{q}) \nabla u^0) + k^2 (\boldsymbol{\nu} \cdot \mathbf{q}) u^0, \qquad \text{on } \mathbf{s} \tag{42}$$

where $\boldsymbol{\nu}$ denotes the outer unit normal vector on $\mathbf{s}$, and ∇ denote the tangential gradient on $\mathbf{s}$.

Using Proposition 1, Corollary 1 can be easily modified to deal with TE polarization if we replace $\mathbf{q}$ in (42) with $\mathbf{b}_j$, where $\mathbf{b}_j$ denotes the jth basis function in the parameterization (8). Then, the global confidence regions can be constructed similarly.

The comparison of the global confidence regions for TE and TM polarization contains computational ingredients, and we leave it for further study.

VIII. Conclusion

We have analyzed a 2-D parametric formulation of nonlinear inverse scattering problems. These problems are nonlinear and severely ill-posed, as they involve the identification of unknown boundary conditions for the Helmholtz equation. Such problems arise in a variety of radar imaging problems of interest to us, including passive radar imaging. We presented a new algorithm to compute Cramér–Rao bounds on shape estimation. This is achieved by employing the domain derivative technique which can be computed numerically using the layer approach and the Nyström method. The resultant CRBs were used to define an asymptotic global confidence region, centered around the true boundary, in which the boundary estimate lies with a prescribed probability. These global confidence regions conveniently display the uncertainty in various geometric parameters such as shape, size, orientation, and position of the estimated target, and facilitate geometric inferences. Numerical simulations showed that our algorithm is very accurate and can be successfully used for performance evaluation of parametric target shape and location estimation problems in passive radar systems.

APPENDIX A
PROOF OF COROLLARY 1

The proof is a slight modification of the proof for star-like boundaries given in [20]. Let $i \in \{1, \ldots, N\}$ and $j \in \{1, \ldots, J\}$ be fixed, and $\mathbf{e}^{(j)}$ be the jth unit vector in $\mathbb{R}^J$. Consider the deformed shape $\mathbf{s}_{\epsilon \mathbf{b}_j}$ given by $\mathbf{s}_{\epsilon \mathbf{b}_j} = \mathbf{s}(t) + \epsilon \mathbf{b}_j(t)$. Then

$$\frac{1}{\epsilon}\left[\mathcal{F}_i\left(\boldsymbol{\phi} + \epsilon \mathbf{e}^{(j)}\right) - \mathcal{F}_i(\boldsymbol{\phi})\right] = \frac{1}{\epsilon}[\boldsymbol{\mathcal{F}}(\mathbf{s}_{\epsilon \mathbf{b}_j})(\mathbf{x}_i) - \boldsymbol{\mathcal{F}}(\mathbf{s})(\mathbf{x}_i)]. \tag{A.1}$$

Since $\mathbf{b}_j(t)$ is continuously twice-differentiable, for sufficiently small ϵ, the deformation $\mathbf{s}_{\epsilon \mathbf{b}_j}$ is also of class C^2 [20]. Therefore, by Theorem 1, as $\epsilon \to 0$, the right-hand side of (A.1) converges to $u_j'(\mathbf{x}_i)$ which solves the exterior Dirichlet problem with boundary data (30). At the same time, the left hand side of (A.1) converges to $\partial \mathcal{F}_i(\boldsymbol{\phi})/\partial \phi_j$, so that $\partial \mathcal{F}_i(\boldsymbol{\phi})/\partial \phi_j = u_j'(\mathbf{x}_i)$.

APPENDIX B
REGULARITY CONDITIONS FOR CRAMÉR–RAO INEQUALITY

It is known that subject to regularity conditions the variance of any unbiased estimate is bounded from below by the Cramér–Rao lower bound (CRB) [40], [41]. For the Gaussian observational model (9), $\mathbf{Y}$ is distributed as

$$p_{\boldsymbol{\phi}}(\mathbf{y}) = (2\pi)^{-N}(\det \mathbf{C}_{\mathbf{W}})^{-1} \cdot \exp\left(-\frac{\|\mathbf{y} - \boldsymbol{\mathcal{F}}(\boldsymbol{\phi})\|^2_{\mathbf{C}_{\mathbf{W}}^{-1}}}{2}\right). \tag{B.1}$$

Let Λ and Γ denote the parameter space and observation space, respectively, i.e., $\boldsymbol{\phi} \in \Lambda$ and $\mathbf{y} \in \Gamma$. This appendix shows that the probability density function (B.1) satisfies the required regularity conditions [40]:

R1: $\nabla_{\boldsymbol{\phi}} p_{\boldsymbol{\phi}}(\mathbf{y})$ exists for all $\boldsymbol{\phi} \in \Lambda$.

R2: $\int_\Gamma \nabla_{\boldsymbol{\phi}} p_{\boldsymbol{\phi}}(\mathbf{y})\, d\mathbf{y} = \nabla_{\boldsymbol{\phi}} \int_\Gamma p_{\boldsymbol{\phi}}(\mathbf{y})\, d\mathbf{y}$ for all $\boldsymbol{\phi} \in \Lambda$.

Proof of R1: Since $\exp(\cdot)$ is an analytic function, $\nabla_{\boldsymbol{\phi}} p_{\boldsymbol{\phi}}(\mathbf{y})$ exists if and only if the gradient of the loglikelihood, $\nabla_{\boldsymbol{\phi}} \log p_{\boldsymbol{\phi}}(\mathbf{y})$, exists. The gradient of the loglikelihood is given by

$$\nabla_{\boldsymbol{\phi}} \log p_{\boldsymbol{\phi}}(\mathbf{y}) = 2\mathrm{Re}[\boldsymbol{\mathcal{F}}'(\boldsymbol{\phi})^H \mathbf{C}_{\mathbf{W}}^{-1}(\mathbf{y} - \boldsymbol{\mathcal{F}}(\boldsymbol{\phi}))] \tag{B.2}$$

hence the left hand side term of (B.2) exists if and only if $\boldsymbol{\mathcal{F}}'(\boldsymbol{\phi})$ exists. The existence of $\boldsymbol{\mathcal{F}}'(\boldsymbol{\phi})$ has been already proved by Corollary 1, which concludes the proof.

Proof of R2: For any $\boldsymbol{\phi} \in \Lambda$

$$\int_\Gamma \nabla_{\boldsymbol{\phi}} p_{\boldsymbol{\phi}}(\mathbf{y})\, d\mathbf{y} = \int_\Gamma 2\mathrm{Re}[\boldsymbol{\mathcal{F}}'(\boldsymbol{\phi})^H \mathbf{C}_{\mathbf{W}}^{-1}(\mathbf{y} - \boldsymbol{\mathcal{F}}(\boldsymbol{\phi}))] p_{\boldsymbol{\phi}}(\mathbf{y})\, d\mathbf{y} \tag{B.3}$$

$$= \int_\Gamma 2\mathrm{Re}[\boldsymbol{\mathcal{F}}'(\boldsymbol{\phi})^H \mathbf{C}_{\mathbf{W}}^{-1}(\boldsymbol{\mathcal{F}}(\boldsymbol{\phi}) - \boldsymbol{\mathcal{F}}(\boldsymbol{\phi}))] p_{\boldsymbol{\phi}}(\mathbf{y})\, d\mathbf{y} = 0 \tag{B.4}$$

because (B.1) implies that the mean of the random vector $\mathbf{Y}$, $\int_\Gamma \mathbf{y} p_{\boldsymbol{\phi}}(\mathbf{y})\, d\mathbf{y}$, is equal to $\boldsymbol{\mathcal{F}}(\boldsymbol{\phi})$. Furthermore, $\nabla_{\boldsymbol{\phi}} \int_\Gamma p_{\boldsymbol{\phi}}(\mathbf{y})\, d\mathbf{y} = \mathbf{0}$ since $\int_\Gamma p_{\boldsymbol{\phi}}(\mathbf{y})\, d\mathbf{y} = 1$. This concludes the proof.

Remark: The differentiability condition is not trivial in general, since for an object with an abrupt boundary (such as the one we are considering) the differentiability conditions might be violated (*e.g.*, the case of position estimation for a rectangular pulse in noise). In fact, if the forward problem were modeled with the geometric optics approximation, then the differentiability conditions would fail.

APPENDIX C
PROOF OF PROPOSITION 1

According to Sokolowski and Zolesio [42, pp. 119–121], if the domain D changes with velocity in the outer normal direction v_n, the domain derivative for the Poisson equation

$$\begin{aligned} -\nabla^2 u(\mathbf{x}) &= h(\mathbf{x}), \qquad \mathbf{x} \in \mathbb{R}^2 \setminus \overline{D} \\ \frac{\partial u}{\partial \boldsymbol{\nu}} &= 0, \qquad \text{on } \mathbf{s} \end{aligned} \tag{C.1}$$

is given by the solution u' to the equation

$$-\nabla^2 u'(\mathbf{x}) = h'(\mathbf{x}), \qquad \mathbf{x} \in \mathbb{R}^2 \setminus \overline{D} \tag{C.2}$$

with boundary condition

$$\frac{\partial u'}{\partial \boldsymbol{\nu}} = \nabla \cdot (v_n \nabla u) + v_n h, \qquad \text{on } \partial D \tag{C.3}$$

where ∇ denotes the tangential gradient on ∂D, and h' is the domain derivative of h. The proof in [42, pp. 119–121] is still the same if we set $h = k^2 u$. For the deformation of (27), the velocity in the outer normal direction v_n is given by $v_n = \boldsymbol{\nu} \cdot \mathbf{q}$. This concludes the proof.

ACKNOWLEDGMENT

The authors would like to thank the Passive Radar Systems group at Lockheed-Martin, particularly Dr. R. Lodwig and Dr. R. Taylor, for helpful discussions.

REFERENCES

[1] W. C. Chew, *Waves and Fields in Inhomogeneous Media*, 2nd ed. New York: IEEE Press, 1995.

[2] D. Colton and R. Kress, *Inverse Acoustic and Electromagnetic Scattering Theory*, 2nd ed. Berlin, Germany: Springer-Verlag, 1998.

[3] F. Natterer, *The Mathematics of Computerized Tomography*. New York, NY: Teubner, Stuggart and Wily, 1986.

[4] H. Griffiths and N. Long, "Television-based bistatic radar," *IEE Proc.*, pt. F, vol. 133, pp. 649–657, Dec. 1986.
[5] A. D. Lanterman, "Tacking and recognition of airborne targets via commercial television and FM radio signals," in *Proc. Acquisition, Tracking and Pointing XIII*, vol. 3692, Orlando, FL, Apr. 1999.
[6] H. L. V. Trees, *Detection, Estimation and Modulation Theory—Part III: Radar–Sonar Signal Processing and Gaussian Signals in Noise*. New York: Wiley, 1971.
[7] A. O. Hero, R. Piramuthu, J. A. Fessler, and S. R. Titus, "Minimax estimation computed tomography using high resolution anatomical side information and B-spline models," *IEEE Trans. Inform. Theory*, vol. 45, pp. 920–928, Apr. 1999.
[8] A. J. Devaney and G. A. Tsihirintzis, "Maximum likelihood estimation of object location in diffraction tomography," *IEEE Trans. Signal Processing*, vol. 39, pp. 672–682, 1991.
[9] G. A. Tsihirintzis and A. J. Devaney, "Maximum likelihood estimation of object location in diffraction tomography—Part II: Strongly scattering objects," *IEEE Trans. Signal Processing*, vol. 39, pp. 1466–1470, June 1991.
[10] A. Schatzberg, A. J. Devaney, and A. J. Wittens, "Estimating target location from scattered field data," *Signal Process.*, no. 2–3, pp. 227–237, 1994.
[11] D. J. Rossi and A. S. Willsky, "Reconstruction from projections based on detection and estimation of objects—Parts I and II," *IEEE Trans. Acoust. Speech Signal Processing*, vol. ASSP-32, pp. 886–906, 1984.
[12] S. F. Yau and Y. Bresler, "Worst case Cramér–Rao bounds for parametric estimation of superimposed signals with applications," *IEEE Trans. Signal Process.*, vol. 40, pp. 2973–2986, Dec. 1992.
[13] P. Stoica and A. Nehorai, "MUSIC, maximum likelihood, and Cramér–Rao bound," *IEEE Trans. Acoust. Speech Signal Processing*, vol. 37, pp. 720–741, May 1989.
[14] "Performance study of conditional and unconditional direction-of-arrival estimation," *IEEE Trans. Acoust. Speech Signal Process.*, pp. 1783–1795, Oct. 1990.
[15] A. L. Swindlehurst and P. Stoica, "Maximum likelihood methods in radar array signal processing," *Proc. IEEE*, pp. 421–441, Feb. 1998.
[16] D. J. Rossi and A. S. Willsky, "ML estimation of object size and orientation from projection data," in *Proc. IEEE Intl Conf. Acoust., Speech Sig. Proc.*, vol. 3, 1984.
[17] P. S. Naidu and A. Buvaneswari, "A study of Cramér–Rao bounds on object shape parameters from scattered field," *IEEE Trans. Signal Processing*, vol. 49, pp. 1478–1481, May 1999.
[18] D. J. Rossi, A. S. Willsky, and D. M. Spielman, "Object shape estimation from tomographic measurements—A performance analysis," *Signal Process.*, no. 1, pp. 63–87, 1989.
[19] H. L. V. Trees, *Detection, Estimation and Modulation Theory—Part I: Detection, Estimation, and Linear Modulation Theory*. New York: Wiley, 1968.
[20] A. Kirsch, "The domain derivative and two applications in inverse scattering," *Inverse Problems*, no. 9, pp. 81–96, 1993.
[21] J. C. Ye, Y. Bresler, and P. Moulin, "Asymptotic global confidence regions in parametric shape estimation problems," *IEEE Trans. Inform. Theory*, Aug. 2000.
[22] R. F. Harrington, *Time-Harmonic Electromagnetic Fields*. New York: McGraw-Hill, 1961.
[23] C. H. Wilcox, "A generalization theorem of Rellich and Atkinson," *Proc. Amer. Math. Soc.*, no. 7, pp. 271–276, 1956.
[24] C. T. Zahn and R. Z. Roskies, "Fourier descriptors for plane closed curves," *IEEE Trans. Computers*, vol. C-41, pp. 269–281, Mar. 1972.
[25] E. Persoon and K. S. Fu, "Shape discrimination using Fourier descriptors," *IEEE Trans. Syst. Man Cybern.*, pp. 170–179, Mar. 1977.
[26] C. K. Chui, *Multivariate Splines*. Philadelphia, PA: SIAM, 1988.
[27] G. C. H. Chuang and C. C. J. Kuo, "Wavelet descriptor of planar curves: Theory and applications," *IEEE Trans. Image Processing*, vol. 6, pp. 56–70, Jan. 1996.
[28] P. Wunsch and A. F. Laine, "Wavelet descriptors for multiresolution recognition of handprinted characters," *Pattern Recognition*, no. 8, pp. 1237–1249, 1995.
[29] H. Akaike, "A new look at the statistical model identification," *IEEE Trans. Automat. Contr.*, vol. AC-19, pp. 716–723, Dec. 1974.
[30] G. Schwartz, "Estimating the dimension of a model," *Ann. Statistics*, no. 2, pp. 461–464, 1978.
[31] J. Rissanen, "Modeling by shortest data description," *Automatica*, pp. 465–471, 1978.
[32] A. K. Jain, *Fundamentals of Digital Image Processing*. Englewood Cliffs, NJ: Prentice Hall, 1989.
[33] K. Arbter, "Affine-invariant Fourier descriptors," in *From Pixel to Features*, J. Simon, Ed. Amsterdam, The Netherlands: Elsevier Science, pp. 153–164.
[34] K. Arbter, W. E. Snyder, H. Burkhardt, and C. Hirzinger, "Application of affine-invariant Fourier descriptors to recognition of 3-D objects," *IEEE Trans. Pattern Anal. Machine Intelligence*, pp. 640–647, July 1990.
[35] R. Kress, *Linear Integral Equations*. Berlin, Germany: Springer-Verlag, 1989.
[36] B. O'Neill, *Elementary Differential Geometry*. New York: Academic, 1966.
[37] D. Colton and R. Kress, *Integral Equation Methods in Scattering Theory*. New York, NY: Wiley-Interscience, 1983.
[38] R. Kress, "Numerical solution of boundary integral equations in time-harmonic electromagnetic scattering," *Electromagn.*, pp. 1–20, 1990.
[39] R. Kress and W. Rundell, "A quasi-Newton method in inverse obstacle scattering," *Inverse Problems*, no. 10, pp. 1145–1157, 1994.
[40] M. Kendall and A. Stuart, *The Advanced Theory of Statistics*, 4th ed. New York: MacMillan, 1977.
[41] H. V. Poor, *An Introduction of Signal Detection and Estimation*, 2nd ed. New York: Springer-Verlag, 1994.
[42] J. Sokolowski and J. Zolesio, *Introduction to Shape Optimization: Shape Sensitivity Analysis*. New York: Springer-Verlag, 1991.

Jong Chul Ye (S'97–M'98) received the B.Sc. (*cum laude*) and the M.Sc. degrees in 1993 and 1995, respectively, from Seoul National University, Seoul, Korea, both in control and instrumentation engineering, and the Ph.D. degree in 1999 from Purdue University, West Lafayette, in electrical and computer engineering.

From 1993 to 1995, he was a Research Assistant in the Department of Control and Instrumentation Engineering, Seoul National University, Korea. In 1995 he was employed at the Korea Advanced System Research Instititute as a Research Scientist. From 1996 to 1999, he was a Research Assistant in the School of Electrical Engineering, Purdue University, West Lafayette. In 1999, he joined the Coordinated Science Laboratory, University of Illinois at Urbana-Champaign as a Postdoctoral Researcher. He is currently a Senior Imaging Scientist with the Polaroid Corporation in Wayland MA USA.

Dr. Ye was a recipient of the Korean Government Scholarship Overseas Award (1995–1998), Purdue CS&E Fellowship (1997–1998), Optical Society of America (OSA) New Focus Student Travel Grant Award (1997), and Purdue Ismail Award (1998).

Yoram Bresler (F'99) received the B.Sc. (*cum laude*) and M.Sc. degrees from the Technion, Israel Institute of Technology, in 1974 and 1981 respectively, and the Ph.D. degree from Stanford University, in 1986, all in electrical engineering. From 1974 to 1979 he served as an Electronics Engineer in the Israeli Defense Force. From 1985 to 1987 he was a Research Associate at the Information Systems Laboratory at Stanford University, working on sensor array processing and medical imaging. In 1987 he joined the University of Illinois at Urbana-Champaign, where he is currently a Professor in the Department of Electrical and Computer Engineering and the Bioengineering Program and Research Professor at the Coordinated Science Laboratory. From 1995 to 1996 he spent a sabbatical leave at the Technion, Israel Institute of Technology. His current research interests include multidimensional and statistical signal processing and their applications to inverse problems in imaging.

Dr. Bresler was an Associate Editor for the IEEE TRANSACTIONS FOR IMAGE PROCESSING from 1992 to 1993, and a member of the IEEE Image and Multidimensional Signal Processing Technical Committee in 1994–1998, and currently is on the editorial board of *Machine Vision and Applications*. In 1988 and 1989 he received the Senior Paper Awards from the IEEE Acoustics, Speech, and Signal Processing Society. He is the recipient of a 1991 NSF Presidential Young Investigator Award, the Technion (Israel Institute of Technology) Fellowship in 1995, and the Xerox Senior Award for Faculty Research in 1998. He was named a University of Illinois Scholar in 1999 and was appointed an Associate at The Center of Advanced Studies in 2001.

Pierre Moulin (S'89–M'90–SM'98) received the degree of Ingénieur civil électricien from the Faculté Polytechnique de Mons, Belgium, in 1984, and the M.Sc. and D.Sc. degrees in electrical engineering from Washington University, St. Louis, MO in 1986 and 1990, respectively.

He was a Researcher at the Faculté Polytechnique de Mons from 1984 to 1985 and at the Ecole Royale Militaire in Brussels, Belgium, from 1986 to 1987. He was a Research Scientist at Bell Communications Research in Morristown, NJ, from 1990 until 1995. In 1996, he joined the University of Illinois at Urbana-Champaign, where he is currently an Associate Professor in the Department of Electrical and Computer Engineering and a Research Associate Professor in the Beckman Institute and in the Coordinated Science Laboratory. His fields of professional interest are image and video processing, compression, statistical signal processing and modeling, nonparametric function estimation, information theory, and the application of multiresolution signal analysis, optimization theory, and fast algorithms to these areas.

Dr. Moulin served as an Associate Editor of the IEEE TRANSACTIONS ON INFORMATION THEORY, 1996–1998 and a Guest Associate Editor of the IEEE TRANSACTIONS ON INFORMATION THEORY's 2000 special issue on information-theoretic imaging. He is currently and Associate Editor of the IEEE TRANSACTIONS ON IMAGE PROCESSING and a member of the IEEE IMDSP Technical Committee. He received a 1997 Career award from the National Science Foundation and the IEEE Signal Processing Society 1997 Senior Best Paper award for a 1995 paper on nonorthogonal subband coding.